

1Cloud base height from sky imager and cloud speed sensor

2

3Guang Wang, Ben Kurtz, Jan Kleissl

4Center for Renewable Resources and Integration, Department of Mechanical and Aerospace Engineering,
5University of California, San Diego, United States

6

7

8

9Abstract

10Cloud base height (CBH) is a critical input to short-term solar forecasting algorithms, yet CBH
11measurements are difficult to obtain. Existing methods to detect CBH include radiosondes,
12ceilometers, and the stereographic method. However, these methods are deficient for intra-hour
13forecasting due to high costs or low temporal resolution. While satellite images could overcome
14these limitations, only the cloud top height can be determined from the thermal IR channel. We
15describe the integration of a cloud shadow speed sensor (CSS) with angular cloud speed from a
16sky imager to determine CBH. Furthermore, an improved methodology to determine cloud
17motion vectors from the CSS is presented, which offers lower noise and greater accuracy and
18stability than existing methods. Two months at the UC San Diego campus were used for
19validation against measurements from meteorological aerodrome reports (METAR) and an on-
20site ceilometer. Typical daily root mean square differences (RMSD) are 126 m which corresponds
21to 16.9% of the observed CBH. Normalized RMSD remains below 30% for all days. The daily bias
22is usually less than 80 m which suggests that the method is robust and that most of the RMSD is
23driven by short-term random fluctuations in CBH. Unlike sky image stereography the present
24method can be applied to measurements at a single site making it widely applicable.

25

26

27

28

29

30

31

32

33

34

35

36

37

38

39

40

41

42

43

44

45

Nomenclature

Note that Δt_{ij} and ϕ_{ij} are used with subscripts when referring to a particular sensor pair and without subscripts when referring to a continuous functional fit of the time shift. Also generally v denotes a vector and U denotes a scalar cloud speed. Unless explicitly noted here and in the text for cloud pixel speeds, all cloud speeds have units of m s^{-1} .

θ_m	Sky imager field of view in degrees from the vertical	MCP	Most correlated pair method for cloud speed measurement
θ_{sensor}	Angle offset between sensors on the CSS	n	Number of pixels of the cloud map in one dimension
β	Direction of v_{real} in reference to line (a-c) of CSS	N	Total number of data points
ϕ_{\perp}	Direction of v_{\perp} in reference to line (a-c) of CSS	nRMSD	Normalized root mean square difference
ϕ_{ij}	Angle between the line connecting sensors i and j and line (a-c) of CSS	P_k	Sensor pair number
Δt_{ij}	Time shift of cloud arrival time between CSS sensors i and j	r	Radius of the CSS sensor circle
AGL	Above ground level	R_{ij}	Maximum cross-correlation coefficient of sensor pair $i - j$
AMSL	Height above mean sea level (m)	RMSD	Root mean square difference
CBH_{ceilo}	CBH estimates from the ceilometer	U_{CSS}	CSS cloud speed
$CBH_{CSS+USI}$	CBH derived from CSS cloud speed and USI cloud pixel speed	U_{pixel}	Cloud pixel speed
CBH	Cloud base height	U_{USI}	USI derived cloud speed
CMV	Cloud motion vector	USI	UC San Diego Sky Imager
CSS	Cloud Shadow Speed Sensor	v_{real}	True cloud velocity vector
LCE-CFM	Linear Cloud edge - Curve Fitting Method	v_{\perp}	Component of v_{real} perpendicular to the

46

47

48

491. Introduction

50

51Cloud base height (CBH) plays an important role in many solar energy applications. For example,
52Bright et al. (2015) incorporate CBH to generating synthetic irradiance signals. While an accurate
53source of CBH become less critical in larger-scale forecasting such as satellite image based
54forecasting, it does matter in short-term solar forecasting which is becoming vital in the solar
55industry as solar penetration increases (Yang et al. 2014). As the cloud is observed by the sky
56imager, variations in CBH change the distance between the latitude and longitude of the center
57of the cloud and its shadow on the ground. In addition the physical cloud size (and its shadow
58size) scales linearly with CBH. Hence, incorrect CBHs lead to offsets between modeled and actual
59cloud shadow. In addition, inaccurate cloud speed associated with CBH errors causes errors in
60the estimated arrival time of cloud shadows, which leads to offsets in ramp forecasting.

61

62The most common CBH measurement techniques include radiosondes (Wang and Rossow, 1995)
63and ceilometers (Gaumet et al. 1998; Martucci et al. 2010). A radiosonde is a battery-
64powered [telemetry](#) instrument package that vertically profiles the atmosphere. Although the
65measurement is accurate as it is taken in-situ, the observations are usually taken only twice daily
66at major airports. This frequency is not sufficient for intra-hour forecasting. Ceilometers, as the
67most common CBH observational tool, emit a high intensity near-infrared laser beam vertically. A
68vertical profile of atmospheric backscatter is then obtained and CBH can be computed multiple
69times per minute. Ceilometer CBH measurements are usually reported in meteorological
70aerodrome reports (METAR). While METAR stations report high quality CBH data, limited
71temporal resolution (hourly reports) and spatial heterogeneity in cloud cover and CBH, can cause
72differences between METAR and local CBH. Since the cost of ceilometers is relatively high, their
73application outside of airports is limited in most countries, although ceilometers are standard at
74weather observation stations in the UK.

75

76A few indirect methods of CBH estimation have emerged during the past decade. Killius et al.
77(2015) estimate CBH based on the output of a Numerical Weather Prediction model. CBH
78estimates with ground based infrared measurements (Shaw and Nugent, 2013; Liu et al. 2015)
79were developed based on the monotonic relationship between CBH and downwelling thermal
80infrared radiance. The assumption that clouds are blackbodies leads to an over-estimation of the
81CBHs derived by infrared cloud imagers (Liu et al. 2015). Satellite images (Prata and Turner, 1997;
82Dessler et al. 2006) estimate cloud height with great spatial coverage and resolution, but the fact
83that satellite radiance is primarily a function of cloud top height limits its application in short-
84term solar forecasting. The stereographic method using two or more sky imagers was initially
85proposed by Allmen and Kegelmeyer (1996) and refined by Kassianov et al. (2005). Nguyen and
86Kleissl (2014) further improved stereographic CBH detection and determined CBH using a two-
87dimensional (2D) method for single homogeneous cloud layers and an enhanced three-
88dimensional (3D) method to provide CBH with high spatial resolution. However, the
89stereographic method requires two sky imagers spaced 1.23 km apart and accurate geometric
90calibration of the imaging systems is critical (Urquhart et al. 2015).

91

92The cloud shadow speed sensor (CSS) (Fung et al. 2014) or cloud speed measurements from
93spatially distributed irradiance or power sensors within a power plant (Bosch and Kleissl, 2013)
94offer an alternative to direct CBH measurements when combined with a sky imager. Since the
95cloud pixel speed (or angular cloud speed) determined by the sky imager can be expressed as
96the ratio of cloud speed [m s^{-1}] and CBH, CBH can be computed from collocated sky images and
97cloud motion vectors (CMVs). Hence, accurate CMV estimation is critical to CBH computation.
98While existing CMV methodology was proposed by Bosch et al. (2013), we present an enhanced
99CMV methodology that is more suitable for CBH computation. Some limitations of the approach
100and validation should be disclosed upfront. The CMV as derived from the CSS applies to the
101cloud edge approaching the sun, but cloud pixel speed is determined in the entire field of view
102of the sky imager, resulting in inconsistency in CBH computation. Furthermore, the ceilometer
103measurement used for validation presents temporally averaged CBH at zenith (versus at solar
104zenith for the CSS). Therefore, random differences between computed CBH and ceilometer CBH
105are expected for validation, but biases should be small.

106

107The principal objective of this paper is to propose a method that offers an accurate local CBH for
108sky imager solar forecasting. This method incorporates a cloud speed sensor with an enhanced
109algorithm to a sky imager, and the package provides an affordable and convenient approach to
110estimate CBH compared to a ceilometer. This paper is organized in five sections. The UCSD CSS
111and data availability will be described in Section 2. A new algorithm to derive cloud speed from
112CSS raw data is described in Sections 3.1 and 3.2. Sections 3.3 and 3.4 introduce a method that
113combines CSS and UCSD sky imager (USI) results to determine CBH. Section 4 provides CBH
114validation against an on-site ceilometer. Section 5 provides conclusions on the method,
115applications, and future work.

116

1172. Hardware

1182.1 Instrumentation and setup

119

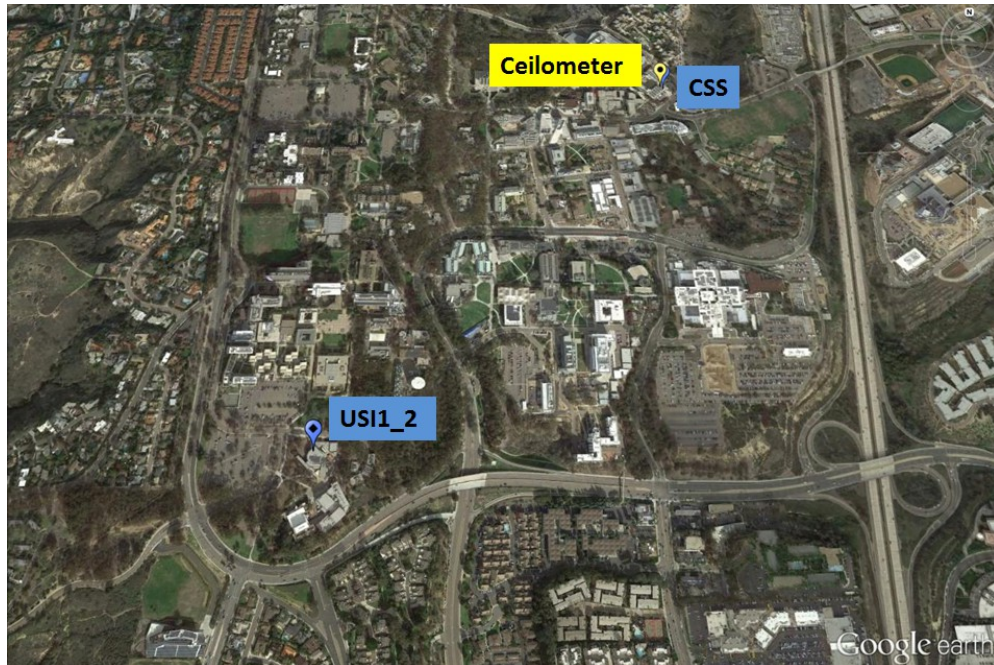
120The CSS (Fung et al. 2014) is a compact system that measures cloud shadow motion vectors
121(CMVs). The system offers an affordable technique to measure CMVs with material costs of less
122than US\$400. It consists of an array of eight satellite phototransistors (TEPT4400, Vishay
123Intertechnology Inc., USA) positioned around an identical phototransistor located at the center
124of a half circle of radius 0.297 m, covering 0-105° in 15° increments (Fig. 1). The sensors have a
125spectral response ranging from approximately 350 to 1000 nm with peak sensitivity at 570 nm.
126Sensor response time was determined experimentally in a laboratory controlled environment
127and was found to be 21 μs rise time (10 - 90% response). High-frequency irradiance data are
128taken from all sensors and fed to a microcontroller (chipKIT Max32, Digilent Inc., USA). The on-
129board static memory allows fast storage of 6,000 10-bit data points per cycle. Due to the high
130sampling frequency, the measurements are not continuous. With the sampling rate of 667
131samples s^{-1} , 6,000 data points fill up the on-board memory in approximately 9 sec. These 9 sec of
132data are then processed to determine one CMV as described in Section 3. During this process,
133the raw data collection has to be temporarily suspended for about 9 sec resulting in a temporal
134resolution of CMVs of about 18 sec. The CMVs used in this analysis were taken from a CSS
135located at 32.8810°N, -117.2328°W, and 106 m height above mean sea level (AMSL) (marked as
136CSS in Fig. 2).

137



138
139 Fig. 1: Cloud Shadow Speed Sensor (CSS) contained inside a weather-proof enclosure with dimensions
140 0.45 x 0.40 m. On the top of the enclosure is an array of nine phototransistors.

141
142 Sky images were taken every 30 sec by a USI located at 32.8722°N, -117.2409°W, 129 m AMSL
143 (marked as USI1_2 in Fig. 2). The USI is designed and developed for short-term solar forecasting
144 applications (Urquhart et al. 2015). It features a high quality imaging sensor and lens contained
145 in a thermally controlled and compact environmental housing. The capture software is employed
146 with a high dynamic range (HDR) imaging technique. Independent measurements of CBH were
147 taken by a Vaisala CT25K ceilometer co-located with the CSS. While all sensors report CBH above
148 ground level (AGL), the elevation of the sensor was added to obtain CBH (AMSL).



150
 151 Fig. 2: Locations of sky imager (USI_2), ceilometer and Cloud Shadow Speed Sensor (CSS) on the UCSD
 152 campus. The straight-line distance between USI and CSS is 1.25 km. Map data ©2015 Google.

153

154 2.2 Data availability

155

156 Since USI data was available continuously, data availability was restricted by the CSS and
 157 ceilometer's operational availability. The CSS was setup on Apr 4 2015. However; intermittent
 158 technical issues occurred until May 1, 2015, when it became fully operational. In order to
 159 comprehensively assess the performance of the CSS during a variety of sky conditions, April 5,
 160 April 20, and the period of May 1 through July 29 were selected for analysis. During this period,
 161 135 of 92 days were clear or contained less than 4 hours of cloud cover per day, and there were
 162 21 overcast or rainy days. Because clear and overcast days do not produce nearly as many ramp
 163 occurrences as partly cloudy days, our study rejects the days with clear or overcast conditions.
 164 Nine additional days had to be eliminated due to missing ceilometer measurements. The
 165 remaining 27 days contain partial cloud cover for at least 4 hours (except July 1 which contains
 166 unusually high clouds for the southern California region which lasted for 2 hours), which are the
 167 conditions of interest for testing CSS performance.

168

169

170 3. Cloud Speed Measurements

171

172 3.1 Prior cloud speed sensor algorithm: Most Correlated Pair Method (MCP)

173

174 While the method of determining CBH is compatible with any measurement of cloud speed, we
 175 also present a new method to obtain cloud speed from the CSS as it had not been documented
 176 before. In the prior CSS algorithm proposed by Bosch et al. (2013), the CMVs were determined
 177 by the Most Correlated Pair Method (MCP). MCP assumes that due to heterogeneity in the cloud

116

12

178 shadow over the area of the sensor, the pair of sensors that lie along the direction of cloud
179 motion will experience the largest cross-correlation as they see the same transect of the cloud
180 (Bosch et al. 2013). Thus, the pair with the largest cross-correlation coefficient is therefore used
181 to determine the direction of cloud motion. The time shift of maximum cross-correlation
182 between the selected pair is then used to calculate the cloud speed. The MCP method suffers
183 from some deficiencies. Most importantly, for the ideal case of a linear cloud edge separating
184 shadow from clear sky, each sensor would see exactly the same signal shape and there would be
185 no single most correlated pair. Instead, the most correlated pair would simply result from
186 arbitrary correlations from sensor noise. Scenarios close to this idealization were found to be
187 common. Since clouds are typically much larger than the spacing between sensors, it seems
188 intuitive that the cloud is nearly homogeneous over the area of the CSS. Thus, CMV results were
189 highly variable. Bosch et al. (2013) addressed the variability through statistical post-processing to
190 determine the most common cloud direction and corresponding cloud speed. The post-
191 processing was shown to be robust and accurate, but the temporal averaging reduced the
192 response of the sensor to sudden changes in cloud velocity. The MCP method also had limited
193 precision as the final direction could only be along individual sensor pairs.

194

195 3.2. Improved cloud speed sensor algorithm: Linear Cloud Edge - Curve Fitting Method (LCE- 196 CFM)

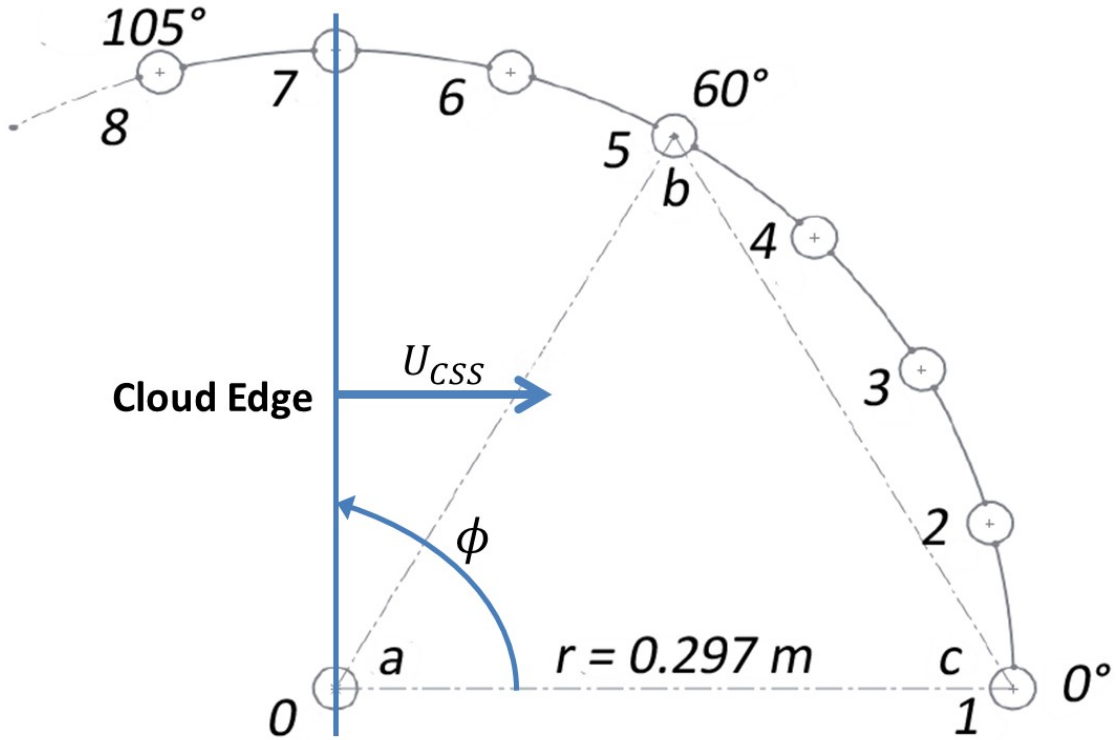
197

198 The assumption in the MCP method is modified to enhance the accuracy and robustness of the
199 method in an operational environment. Because the CSS is small compared to a typical cloud, we
200 can reasonably assume the cloud edge to be linear (Fig. 3). The signal measured by each sensor
201 is then identical except of the temporal deviation between the signals, resulting in a perfect
202 cross-correlation $R_{ij}=1$ (i and j refer to the sensors). Therefore, it is not the
203 magnitude of the cross-correlation that distinguishes the sensor pair aligned with the CMV,
204 rather the time lag associated with the maximum R_{ij} between different sensor pairs provides
205 clues as to the relative alignment of each pair with respect to the CMV. Hence, we will fit a
206 function to the time lag versus sensor-pair direction, and we term this method the "Linear Cloud
207 Edge - Curve Fitting Method".

208

209

210



211

212 Fig. 3: Illustration of the linear cloud edge assumption and LCE-CFM method on top of the CSS luminance
 213 sensor arrangement. Each circle represents a sensor arranged in a circular pattern with 15° spacing about
 214 the central sensor. The sensor pair combinations are constructed with the central sensor and one of the
 215 other sensors for angles from 0° to 105°, e.g., sensor pair combination 0/1 for 0°, 0/2 for 15°, etc.
 216 Additional angles from 120° to 165° are obtained through equilateral triangles between the central sensor
 217 and another sensor pair, e.g., sensor pair combination 1/5 for 120°, 2/6 for 135°, etc. The linear cloud
 218 edge is shown as a blue line and is assumed (for simplicity, but not limiting generality) to be advected
 219 along the line connecting sensors 0 and 1.

220

221 As in the MCP method, the maximum cross-correlation coefficient R_{ij} of each pair of signals
 222 will be determined (Fung et al. 2014) and the associated time shift Δt_{ij} for that pair will be
 223 recorded. Considering a linear cloud edge that is crossing the CSS moving in the direction of the
 224 sensor line (a-c), it is straightforward that:

225

$$226 \quad r \cdot \cos \phi_{ij} = U_{CSS} \cdot \Delta t_{ij} \quad , \quad (1)$$

227

228 where r is the radius of the sensor circle, ϕ_{ij} is the cloud edge direction that is defined as
 229 the angle between the line connecting sensors i and j and the line (a-c). i and j
 230 vary from 0 to 8, but only 12 sensor pair combinations i / j (0/1, 0/2, 0/3, 0/4, 0/5, 0/6,
 231 0/7, 0/8, 1/5, 2/6, 3/7, 4/8) are used in our configuration. ϕ_{ij} can be expressed as (

232 $360^\circ - p_k \times 15^\circ$) where p_k is the sensor pair number ($k = 0$ to 11 following the
 233brackets in the previous sentence). U_{CSS} is the speed of the cloud edge, i.e. cloud speed.
 234With distance r and cloud speed U_{CSS} being constant for each pair, the time shift Δt_{ij}
 235becomes a function of $\cos \phi_{ij}$. The trigonometric relation holds for all cloud edge directions
 236as the cloud velocity is assumed to be perpendicular to the cloud edge. For the sensor pairs
 237without the central sensor, Eqn. 1 still holds as long as the selected sensor i and the sensor
 238 j lie on one side of an equilateral triangle constructed from the central sensor, sensor i
 239and sensor j . Because the time shift Δt_{ij} returned by the CSS can be either positive or
 240negative depending on the cloud direction, 12 sensor pairs are sufficient to cover 360° in 15°
 241increments.

242

243

244For the ideal assumption of a linear cloud edge, plotting Δt versus ϕ would therefore be
 245expected to produce a cosine function. For verification, the cosine function is used to fit the
 246 Δt_{ij} versus ϕ_{ij} points for each 9 sec measurement, and the R^2 value is employed to
 247determine the goodness of the fit (Fig. 4). A high R^2 supports the linear cloud edge
 248assumption. Since the linear cloud edge assumes that the velocity is perpendicular to the cloud
 249edge, the sensor pair aligned with the CMV is farthest apart along the CMV at distance r .
 250Thus, the maximum of the cosine function which represents the longest time shift Δt should
 251occur at the CMV direction. While the side effect of LCE assumption is not explicitly visible in the
 252results, the potential limitation and future improvement of LCE assumption are discussed in
 253section 4.3. The cloud speed then becomes the ratio of the distance r and the time shift
 254 Δt :

255

$$256 \quad U_{CSS} = \frac{r}{\Delta t} . \quad (2)$$

257

258Note that the cosine model fit to Eqn. 1 should be constrained to return solutions with $\Delta t >$
 2590. Fig. 4 illustrates this procedure using 9 sec of luminance data. The correlations between all
 260sensor pairs are very large (>0.999), which causes issues in the robustness of the MCP method.
 261On the other hand, the linear cloud edge assumption is validated through a high R^2 value
 262(0.99) which indicates that the time shift is indeed a strong function of the cosine of the
 263direction. As a result the CMV direction and speed can be obtained with confidence using Eqn. 2.

264 In the example in Fig. 4 the time shift is determined as $\Delta t = 0.104$ s, and the corresponding
 265 direction is $\phi = 323^\circ$ yielding a cloud speed $U_{CSS} = 2.87 \text{ m s}^{-1}$ as per Eqn. 2.

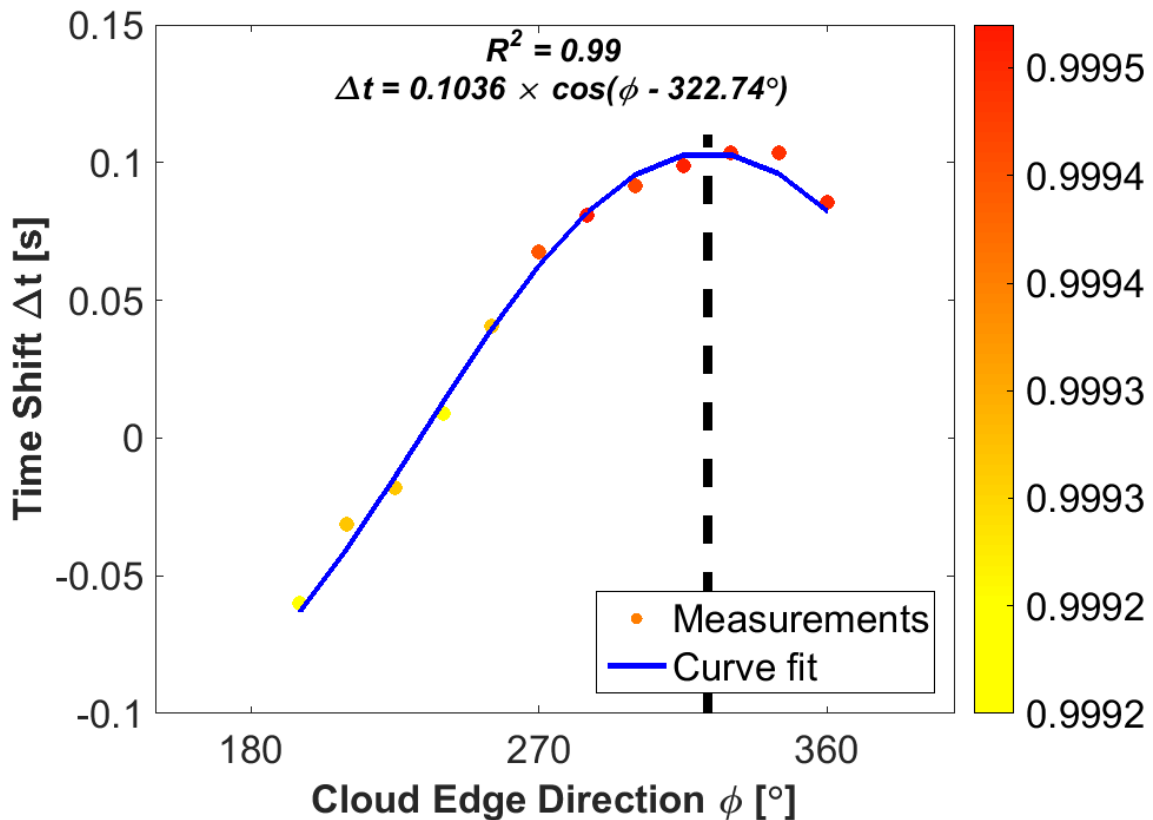
266

267 A filter is applied for data quality control: If the average R_{ij} is less than 0.9 or R^2 of the
 268 cosine curve fit is less than 0.9, the CMV will not be computed. Small R_{ij} is likely a result of
 269 no cloud passage or dynamic clouds. A small R^2 indicates poor curve fitting and therefore an
 270 unreliable result. Generally partly cloudy conditions result in numerous valid CMVs while
 271 homogeneous cloud conditions (e.g., clear and overcast) result in infrequent valid CMV output
 272 due to small R_{ij} . Typically, 1700 raw data sets are recorded during an eight hour analysis day,
 273 and about 110 CMVs are delivered for an overcast day and less than 10 CMVs for a clear day. For
 274 partly cloudy days, about 400 CMVs pass the quality control, which is equivalent to one CMV
 275 value every 50 sec. The sampling rate is sufficient for cloud motion estimation.

276

277

278



279

280 Fig. 4: Illustration of the LCE-CFM to determine CMVs on May 31, 2015 at 17:16:19 UTC. The x-axis
 281 represents direction ϕ that is equal to $(360^\circ - p_k \times 15^\circ)$, where p_k is the sensor pair number (

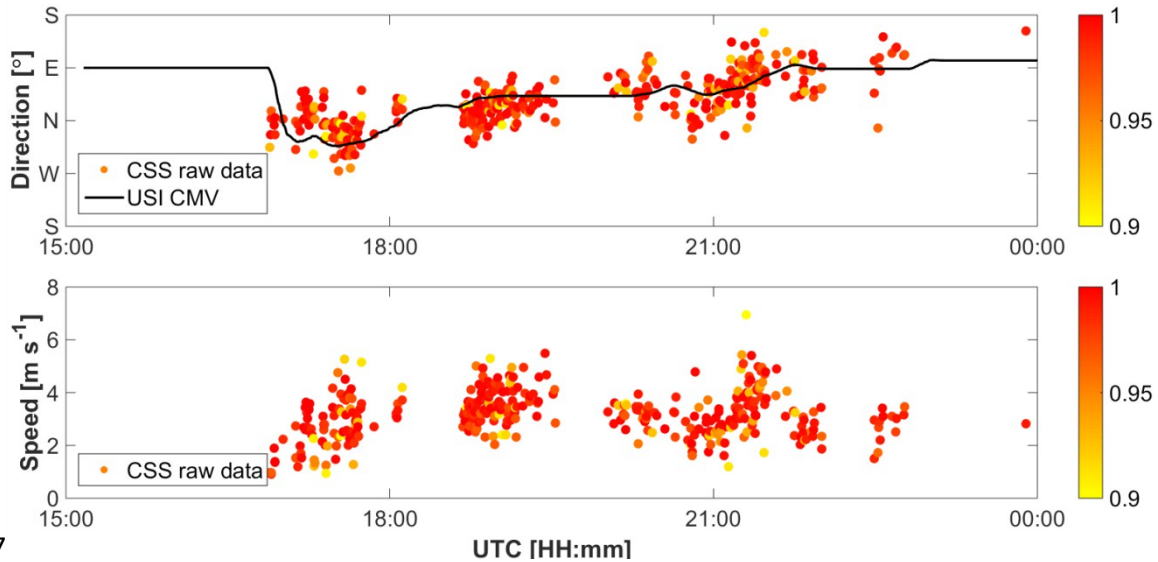
282 $k = 0$ to 11). The y -axis represents the time shift Δt , and the color indicates the strength of
 283 correlation R_{ij} . The curve indicates the best fit of $\Delta t = 0.103 \times \cos(\phi - 322.7^\circ)$. The
 284 maximum time shift of the cosine function is selected as the direction of cloud motion as indicated by the
 285 vertical dashed black line.

286

287 Fig. 5 shows a set of CMVs for one day together with filtered CMV direction determined by the
 288 USI as an independent validation. Clouds are moving northward at 1 to 6 m s^{-1} changing to
 289 eastward as the day progresses. The USI direction generally falls in the center of the CSS raw
 290 data points indicating good agreement. There is some variability in CSS raw data, which is likely a
 291 result of both physical cloud dynamics and sensor noise. The same trends are seen in the wind-
 292 rose plot for CSS data on this day in Fig. 6; most of CMVs cluster in the north-east-ward direction
 293 with an average speed range of 2 to 6 m s^{-1} . Additional validation of the LCE assumption is
 294 presented in Appendix A1.

295

296

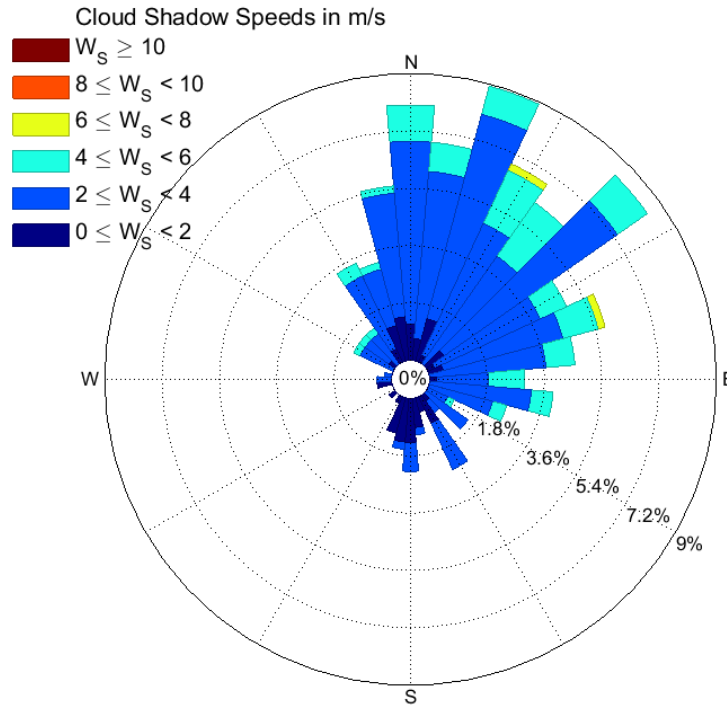


297

298 Fig. 5: Cloud direction (defined as direction the cloud is moving towards) and cloud speed determined by
 299 the LCE-CFM using CSS data on May 31, 2015. Each circle represents one CMV computed based on 9
 300 seconds of measurements and the color provides the R^2 value for the curve fit of 9-second
 301 measurements. The black line presents an independent validation of cloud direction using the CMV
 302 determined from the USI. Since cloud speed in m s^{-1} cannot be determined from the USI alone, there is no
 303 validation data in the lower graph.

304

305



306
307

308 Fig. 6: Wind-rose plot of cloud direction and cloud speed of the data shown in Fig. 5. The color bins show
309 cloud speed range, and the values on concentric circles represent the frequency of appearance of each
310 cloud speed bin.

311 In summary, compared to the prior MCP method, the LCE-CFM yields two distinct advantages: (i)
312 more clustered, i.e. robust, CMV results without post-filtering, and (ii) continuous cloud direction
313 output compared to the 15 (equivalent to the angular arrangement of the sensors)

314 discretized output for the MCP method. To demonstrate the improvement of the LCE-CFM, an
315 example of the prior MCP method is provided in Appendix A2. The disadvantage is that the LCE-
316 CFM calculates correlation for all sensor pairs, whereas the MCP method can bypass the
317 calculation for poorly correlated pairs. This triples the computational time on the CSS
318 microcontroller to 40 sec. Therefore, for this application, the processing was performed on a
319 remote Intel I5 workstation instead, which decreases computational time by more than an order
320 of magnitude.

321
322

323 3.3 Cloud pixel speed from USI data

324

325 In this section, we will first introduce the sky imager cloud motion algorithm, and based on that
326 in conjunction with the CSS cloud speed, a local CBH will be determined. The USI can be used to
327 detect clouds and obtain cloud pixel speed. These measurements yield forecasts of future cloud
328 locations at high spatial and temporal resolutions and can improve forecast skill up to a 20 min
329 forecast horizon. The benefit of using sky imager observations over a large ground sensor
330 network is that only one or a few instruments deployed around the area of interest are capable
331 of determining the current distribution of cloud cover at a high resolution. The forecast
332 procedure is outlined in the flow chart in Fig. 7. The USI forecast procedure is briefly explained
333 within this section. It is very similar to other standard forecast procedures, such as those

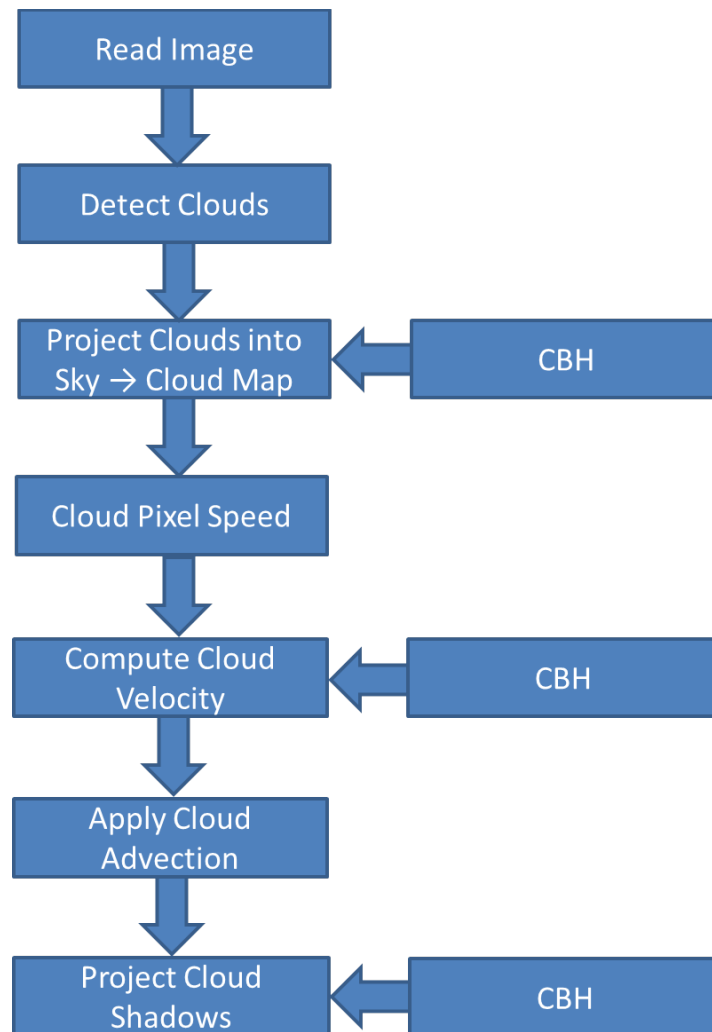
334 presented by Cazorla Cabrera (2010) and Schmidt et al. (2015). For more details on the USI
335 forecast, consult Chow et al. (2011), Ghonima et al. (2012), and Yang et al. (2014).

336

337

338

339



340

341 Fig. 7: Flowchart of the sky imager solar forecast procedure. CBH is used to project clouds onto a cartesian
342 sky coordinate system, to obtain cloud speed, and to project the advected cloud shadows to the ground.

343

344 Cloudy pixels are detected using spectral information from the RGB images. CBH is then used in
345 conjunction with lens geometry to map these clouds to a latitude-longitude grid at the CBH
346 creating the cloud map (Chow et al. 2011). In absence of local data, CBH is taken from the closest
347 METAR. Cloud pixel velocity is obtained by applying the cross-correlation method (CCM, Chow et
348 al. 2011) to the RBR of two consecutive cloud maps. The cloud velocity [m s^{-1}] is then calculated
349 by converting from cloud pixel speed [pixel s^{-1}] to cloud shadow speed using a velocity scaling
350 factor which is a function of CBH (see Eqn. 3 later). Note that since the distance from sun to
351 earth is much larger than the distance from cloud to earth, the cloud shadow speed is assumed
352 to equal the cloud speed for all solar zenith angles.

2513

26

3533.4 Cloud base height determination from CSS and USI (CSS+USI method)

354

355In this section, we introduce the mathematical algorithm (CSS+USI) that obtains the CBH for sky
356imager forecasting from CSS cloud speed measurements. Fig. 8 introduces the geometrical terms
357on a cloud map. In the USI forecast, cloud velocity is calculated by converting from cloud pixel
358speed to equivalent m s^{-1} cloud speed as:

359

$$360 \quad U_{USI} = U_{pixel} \times \frac{CBH \times 2 \tan \theta_m}{n}, \quad (3)$$

361

362where U_{USI} is cloud speed in units of m s^{-1} and U_{pixel} is image-average cloud pixel speed
363in units of pixel s^{-1} obtained through the cross-correlation method applied to two consecutive
364USI images. The last term in Eqn. 3 represents a velocity scaling factor, in which θ_m is the
365maximum view angle of the USI measured from zenith (here $\theta_m = 80^\circ$), $CBH \times 2 \tan \theta_m$

366is the horizontal length of the sky imager view domain (termed “cloud map”), and n is the
367number of pixels of the cloud map in one dimension (Fig. 8). Therefore, the velocity scaling
368factor has units of m pixel^{-1} . Note that the pixel size of the cloud map is distinct from the pixel
369size in the original sky image.

370

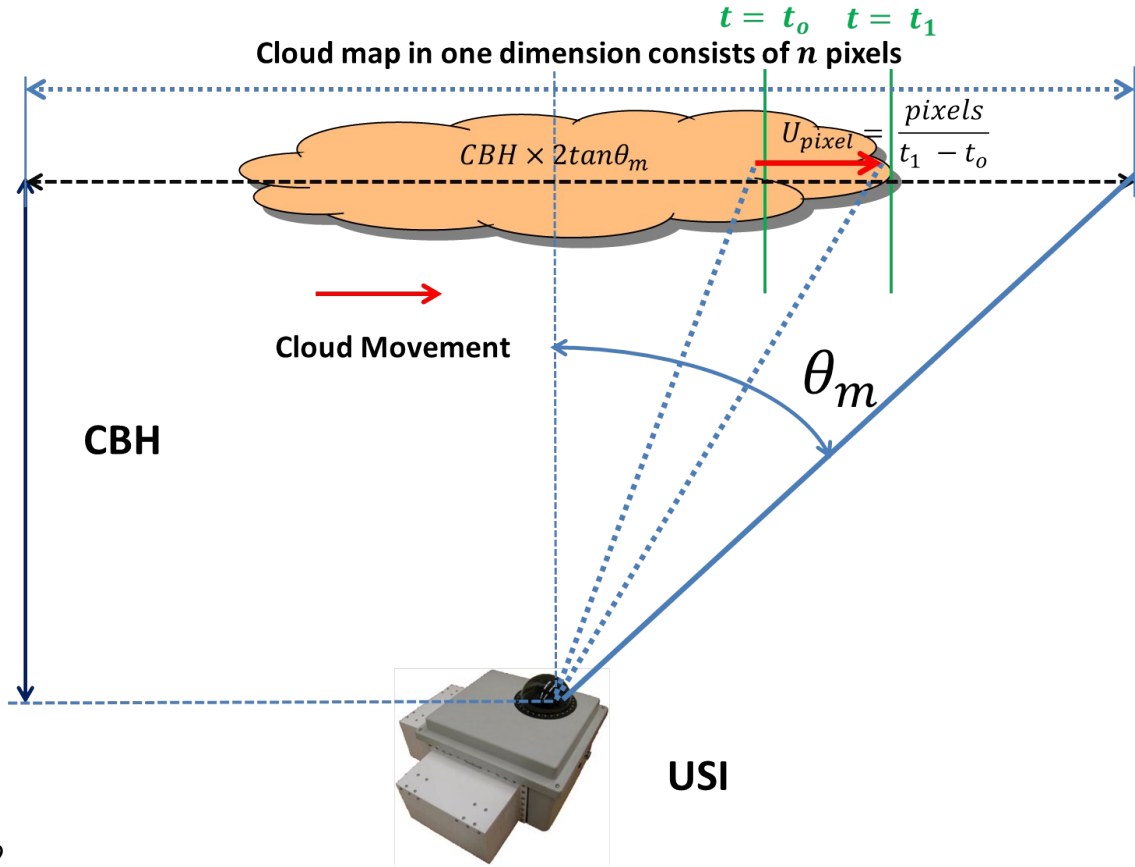
371In Fig. 8, the cloud observed by the USI moves from time $t=t_0$ to $t=t_1$ and U_{pixel} is
372computed from the number of pixels that the cloud moves during the period $t_1 - t_0$. The

373cloud map consists of $n \times n$ pixels, i.e. n is the number of pixels of the cloud map in
374one dimension. Its physical size is computed with the trigonometric expression
375 $CBH \times 2 \tan \theta_m$. So the term $\frac{CBH \times 2 \tan \theta_m}{n}$ refers to the physical distance per pixel of

376the cloud map. With the cloud speed expressed as the number of pixels per second, U_{USI}

377can be calculated according to Eqn. 3.

378



379

380 Fig. 8: Illustration of the geometrical and kinematic relations between cloud pixel speed U_{pixel} , cloud
 381 speed determined by USI U_{USI} , maximum view angle of the USI θ_m and CBH.

382

383

384 Eqn. 3 indicates how to obtain cloud speed in $[m\ s^{-1}]$ from CBH and the USI derived cloud pixel
 385 speed. Conversely, with independent measurements of cloud speed from the CSS, U_{CSS} , we

386 can back-calculate the local CBH (labeled as $CBH_{CSS+USI}$) by replacing U_{USI} with

387 U_{CSS} in Eqn. 3 to yield:

388

389
$$CBH_{CSS+USI} = \frac{U_{CSS}}{U_{pixel}} \times \frac{n}{2 \tan \theta_m} . \quad (4)$$

390

391 It can be observed that CBH depends on the ratio of U_{CSS} and U_{USI} . Eqn. 4 is
 392 implemented into the USI forecast algorithm to calculate local CBH at each step using the most
 393 recent CSS measurement. The method is called CSS+USI and the detailed pseudocode and a
 394 flowchart of the method are available in Appendix A3.

395

396A 10 min window median filter was applied to the time series of CBH from the CSS+USI method.
 397Due to the small sampling area (a small cone above the ceilometer), heterogeneous cloud
 398shapes, and cloud formation and movement, the raw 20 sec ceilometer data is too variable and
 399is not representative of the CBH in the field of view of the USI. Therefore, consistent with
 400Nguyen and Kleissl (2014) when the CSS+USI method yields a $CBH_{CSS+USI}$ at the USI
 401timestamp, a 15 minute median filter centered on that timestamp is applied to ceilometer
 402measurement. In this way, only the dominant ceilometer cloud layer is captured to compare with
 403the filtered results of the proposed CSS+USI method.

404

4054. Cloud base height validation

406

4074.1 Aggregate CBH statistics

408

409The CBH validation is presented in this section. The CSS+USI method is validated against METAR
 410and an on-site ceilometer on the available days listed in Table 1. Two error metrics were used to
 411characterize the performance of the method: root mean square difference (RMSD) and
 412normalized RMSD.

413

$$414 \quad RMSD = \sqrt{\frac{1}{N} \sum_{k=1}^N (CBH_{CSS+USI} - CBH_{ceilo})^2}, \quad (5)$$

415

416where N is the total number of data points. RMSD is divided by the daytime average CBH to
 417obtain the normalized RMSD (nRMSD). Note that although both RMSD and nRMSD are used to
 418evaluate the method, RMSD is relevant for the correct prediction of the timing of a ramp event.

419

420The performance of the proposed method is summarized in Table 1 and Fig. 9 for a range of
 421cloud types, cover fractions, heights, and layers that existed on these days. Generally low
 422cumulus and low stratus clouds prevailed, but high cirrus clouds were observed on July 1, and
 423May 22 featured altocumulus clouds. The best performance occurred on July 24 with the RMSD
 424as low as 21 m (6.2% nRMSD), with the daily RMSD remaining below 130 m. The daily biases are
 425usually less than 80 m and the overall bias is only 23 m indicating that most of the RMSD is
 426driven by shorter-term random fluctuations that are difficult to model. Also, an unusual day with
 427high cirrus for only two hours was observed on July 1, 2015, so we were able to demonstrate the
 428performance of the method in different conditions. Thin clouds tend to have more diffused
 429edges which may weaken the linear cloud edge assumption and the ability to obtain high
 430correlations between different sensors. Nevertheless, the method still captures the CBH with a
 431RMSD of 830 m that corresponds to an nRMSD of 14.2% given the large CBH. On the other hand,
 432METAR delivers CBH with large differences to local CBH and ceilometer, which demonstrates the
 433spatial variability in cloud coverage due to the climate difference as the METAR site is located 8.8
 434km further inland, while the CSS is only 1 km from the coastline (These spatial differences would
 435likely be smaller at flat continental sites). In fact, the CSS-USI CBH delivers better CBH than
 436METAR on all days in this study. The proposed CSS+USI method is therefore expected to be
 437superior to METAR CBH in short term solar forecasting.

438

439Note that the sky imager cloud pixel velocity represents all cloud edges in the entire sky image,
440while the CSS measurement represents a single cloud edge approaching the sun. However, we
441assume that those two measurements refer to the same cloud edge when applying Eqn. 4 and
442the effect of the assumption limits the CBH accuracy. In addition, the ceilometer measurement in
443our validation represents temporally averaged CBH at zenith, while CSS+USI CBH represents
444spatially averaged CBH. Therefore, random differences between ceilometer CBH and CSS-USI
445CBH are expected. In summary, the method was generally accurate for low clouds and although
446it is rare to observe alto-cumulus and cirrus clouds in coastal southern California, May 22 and
447July 1 confirmed the robustness of the method under those conditions.

448

449

450

451Table 1: Daytime average ceilometer, METAR, and CSS-USI cloud base height and difference
452metrics between ceilometer and CSS+USI. The last line provides the average of the entries in the
45327 rows.

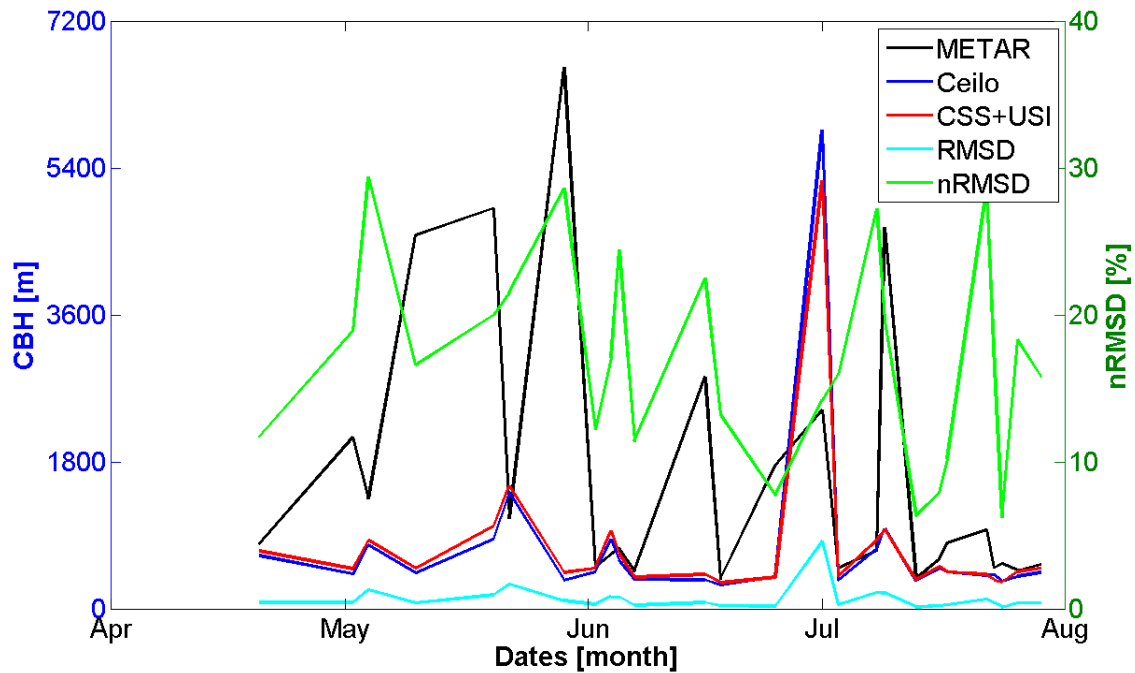
Date [YYYYMMDD]	METAR [m]	Ceilometer CBH [m]	$CBH_{CSS+USI}$ [m]	RMSD [m]	nRMSD [%]
2015-04-05	3536	788	848	108	13.7
2015-04-20	793	650	707	76	11.7
2015-05-02	2101	424	490	80	18.9
2015-05-04	1346	782	841	230	29.4
2015-05-10	4577	441	495	73	16.6
2015-05-20	4904	851	1013	170	20.0
2015-05-22	1107	1421	1500	305	21.5
2015-05-29	6631	350	443	100	28.6
2015-06-02	504	450	498	55	12.2
2015-06-04	670	849	948	145	17.1
2015-06-05	740	595	680	145	24.4
2015-06-07	460	359	385	41	11.4
2015-06-16	2840	355	420	80	22.5
2015-06-18	365	288	320	38	13.2
2015-06-25	1759	390	386	30	7.69
2015-07-01	2438	5864	5245	830	14.2
2015-07-03	498	345	398	55	15.9
2015-07-08	708	736	841	200	27.2
2015-07-09	4676	979	976	192	19.6
2015-07-13	374	348	358	22	6.32
2015-07-16	609	494	521	39	7.89
2015-07-17	806	450	452	46	10.2
2015-07-22	965	411	420	117	28.5
2015-07-23	500	415	355	68	16.4
2015-07-24	550	340	332	21	6.21
2015-07-26	470	400	458	73	18.3
2015-07-29	540	444	495	70	15.8
All Days	1683	748	771	126	16.9

454

3317

34

455



456

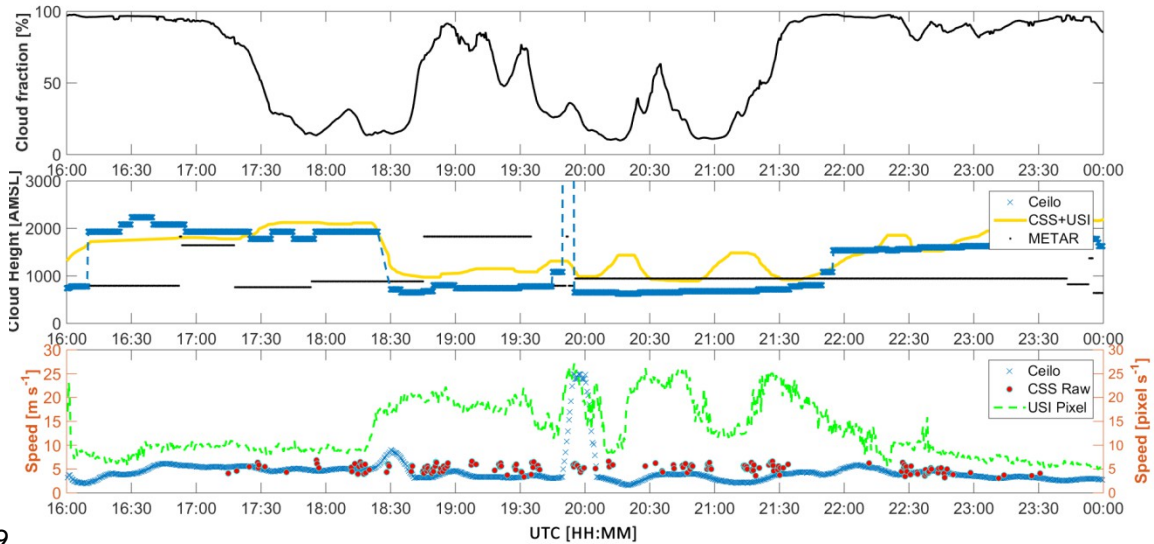
457 Fig. 9: Comparison of daytime average CBH from METAR, Ceilometer, and CSS+USI. RMSD between
458 CSS+USI and ceilometer are also shown. See Table 1 for detail.

459 4.2 CBH validation examples for two days

460

461 Two detailed examples are analyzed in this section to further illustrate and explain the
462 performance of the CSS+USI method. Fig. 10 shows the CBH comparison of ceilometer
463 measurements, METAR, and the CSS+USI method for May 22, a day with different cloud types
464 and multiple cloud layers. The period from 16:00 to 17:30 UTC is characterized by nearly
465 overcast stratus clouds at 2,000 m AMSL that turn into alto-cumulus at the same altitude. During
466 18:30-21:45 UTC, scattered cumulus dominate, while after 21:45 UTC, broken cumulus are
467 observed. UTC lags local standard time (PST) by 8 hours.

468



469

470 Fig. 10: Sample comparison among different CBH measurements during the daytime of May 22, 2015. See
 471 Fig. 2 for locations of the instruments. Top: USI cloud fraction in units of %. Middle: CBH comparison
 472 between local ceilometer measurements (blue crosses), and the proposed CSS+USI method described in
 473 Section 3 (yellow line). The black dots indicate the measurement from airport METAR at Miramar Naval Air
 474 Station (KNKX), 8.8 km to the east of ceilometer. Bottom: Cloud speed determined by the CSS and USI. The
 475 green dashed line shows U_{pixel} (right y-axis). The blue line represents the cloud speed U_{USI} in m
 476 s^{-1} calculated by Eqn. 3 with the CBH input from the local ceilometer measurements, while the red dots
 477 show the raw measurements from CSS. The USI pixel speed is not expected to match, but the other two
 478 methods are expected to match. Note that the brief period of $\sim 25 \text{ m s}^{-1}$ USI+Ceil cloud speed at 20:00 UTC
 479 is a result of ceilometer measurements of CBH = 7,500 m which are cut off the middle graph for readability
 480 of the CBH variation.

481

482

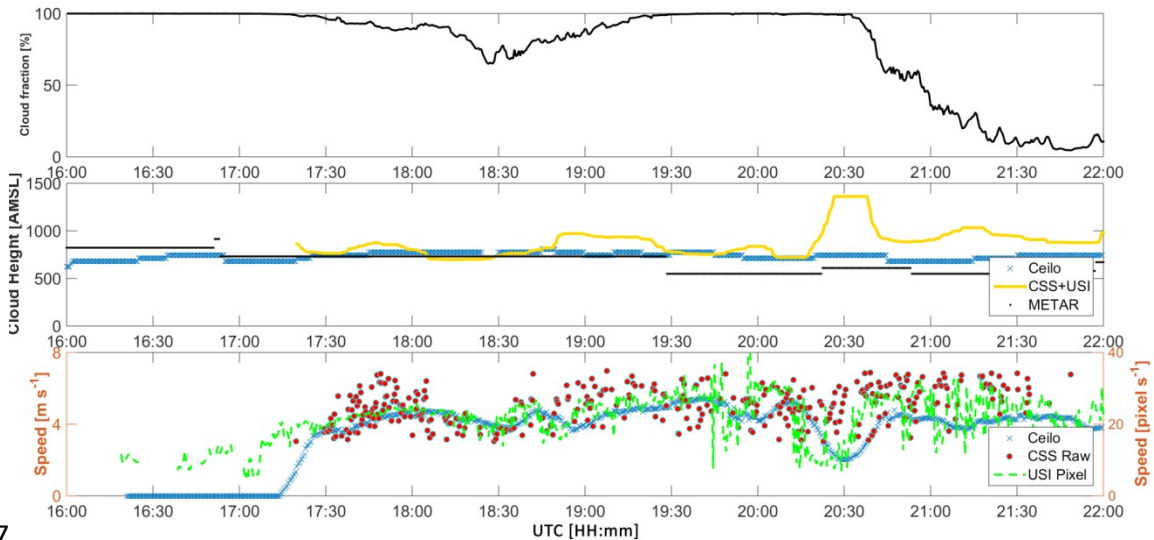
483 In the middle plot of Fig. 10, both CBH from local ceilometer measurements (the ground truth)
 484 and the CSS+USI method yield the same trend. For example, between 16:00-18:30 UTC, the
 485 CSS+USI method produces similar CBHs as the local ceilometer at about 2,000 m, while METAR
 486 reports 800 m which substantiates the concerns about using off-site METAR CBH data. At 18:30
 487 UTC, ceilometer measurements indicate a CBH transition from about 2,000 m to 750 m, and the
 488 CBH from the CSS+USI method follows this transition, although with about a 300 m offset. After
 489 20:00 UTC, an additional cloud layer with a different direction and variable speed, temporarily
 490 confuses the $CBH_{CSS+USI}$, as evident in a briefly elevated CBH around 20:15 UTC, 21:15 UTC
 491 and 22:15 UTC. However, the CSS+USI method still captures the CBH transition detected by the
 492 ceilometer from 800 m to 1,500 m at 22:00 UTC, and follows the ceilometer measurement until
 493 the end of the day. Again, METAR CBHs differ after 22:00 UTC indicating spatial heterogeneity in
 494 CBH. In summary, the CSS+USI method is accurate on this day especially in the morning. The
 495 daily RMSD is 305 m and nRMSD is 21.5%.

496

497 July 8 is analyzed in Fig. 11 as an example of a day with one of the largest observed nRMSD
 498 (27.2%). On this day, there are unusual fluctuations in cloud pixel speed reported from 19:30
 499 UTC to 22:00 UTC, especially a brief period of significantly smaller pixel speeds around 20:30
 500 UTC, which causes a large CBH peak at that time. Visual inspection of the cloud images indicates

501 that these fluctuations are not representative of the actual cloud motion, though the exact
 502 reason that the USI motion algorithm performs poorly is unclear. Regardless, this illustrates again
 503 that the accuracy of the CBH estimate depends on the quality of cloud vectors from both the USI
 504 and the CSS.

505
 506



507
 508 Fig. 11: Same as Fig. 10, but for July 8 illustrating a case when unstable cloud pixel speed determination
 509 causes a large offset of local CBH estimates.

510

511 4.3 Assumptions and limitations

512

513 In this section, the improvement and possible reasons for CBH errors are further discussed. Its
 514 performance is further compared to a prior method introduced by Bosch et al. (2013).

515

516 As implemented in section 3.2, the LCE assumption implies that only the component of the
 517 velocity that is perpendicular to the cloud edge is detected. This assumption can cause offsets in
 518 determining CMVs, which is illustrated in Fig. 12. The cloud edge initially shades the central
 519 sensor at $t=t_0$, and then moves in one of two ways until it shades sensor 6. (i) It moves

520 perpendicular to the cloud edge with speed v_1 and reaches sensor 6 at $t=t_1$, which is

521 consistent with LCE assumption. (ii) It moves in a non-perpendicular direction with speed v_2

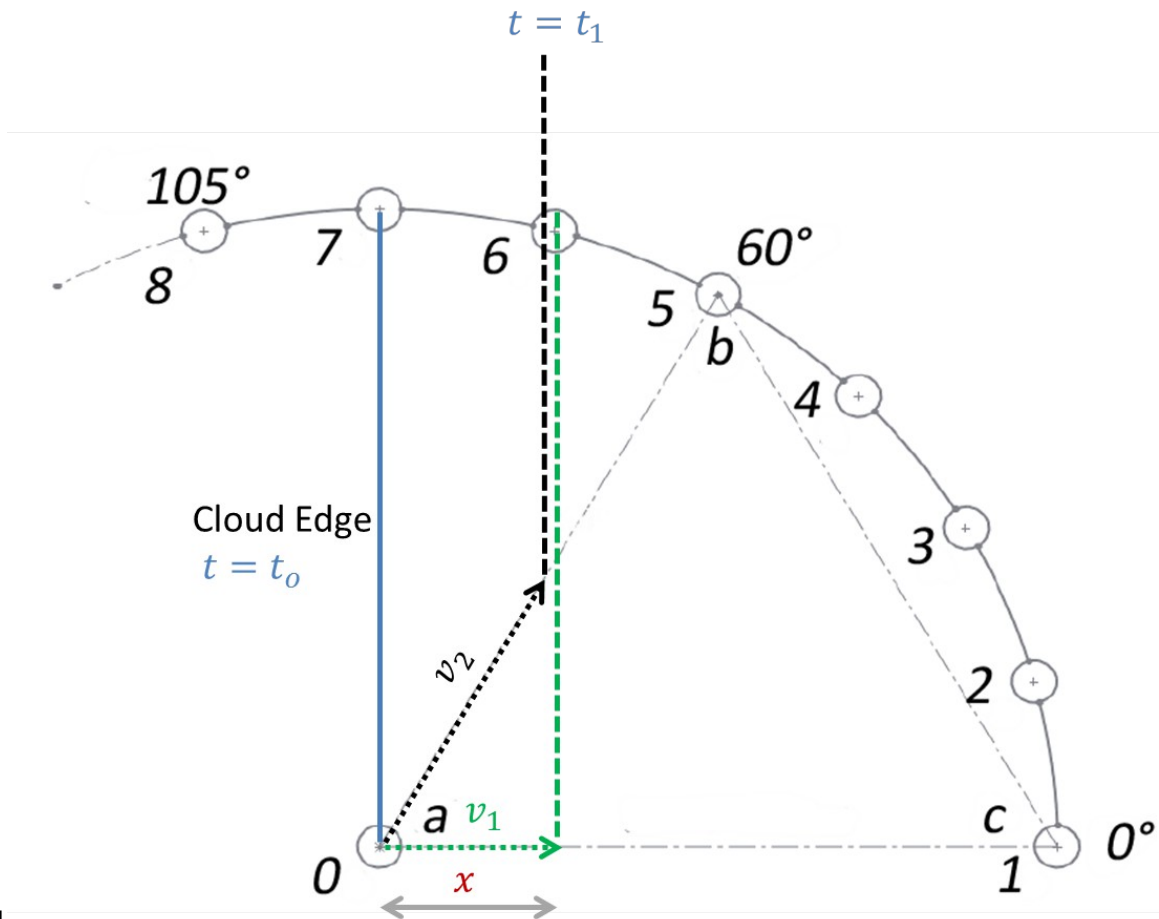
522 whose component normal to the cloud edge is v_1 , and also reaches sensor 6 at $t=t_1$. In

523 these two cases the signal measured by sensor 6 would be identical. Therefore, no matter what
 524 the direction of the CMV, the LCE-CFM will only detect the cloud speed component

525 perpendicular to the cloud edge (here v_1). Thus, if the CMV is not perpendicular to the cloud

526 edge, the cloud speed is underestimated, and subsequently, the lower CSS measurements
 527 causes a lower local CBH according to Eqn. 4. This is the main limitation of the linear cloud edge
 528 assumption.

529
530



531
532 Fig. 12: Illustration of a thought experiment that shows LCE-CFM method can only measure the velocity
533 component perpendicular to the cloud edge due to a limitation of the linear cloud edge assumption. The
534 blue line represents the original cloud edge and the vertical green dashed line represents the future
535 position associated with the CMV v_1 , while the black line indicates the future position associated with
536 the CMV v_2 .

537
538

539 For an infinite linear cloud edge, the cloud positions resulting from v_1 and v_2 in Fig. 12
540 are indistinguishable, while for real (finite) clouds, the cloud positions will be different. Bosch et
541 al. (2013) addressed this ambiguity by assuming that successive clouds passing the sensor move
542 with the same CMV as they are transported by air at the same height in the boundary layer. Two
543 successive clouds that pass the sensor array with CMV v_{real} and different edge orientations
544 will record velocities v_{\perp_1} and v_{\perp_2} , at angles ϕ_{\perp_1} and ϕ_{\perp_2} as shown in Fig. 13. The
545 true velocity v_{real} , can then be found as:

546

$$547 \quad |v_{real}| = \frac{|v_{\perp_1}|}{\cos(\phi_{\perp_1} - \beta)} = \frac{|v_{\perp_2}|}{\cos(\phi_{\perp_2} - \beta)}, \quad (6)$$

548

549 which requires the angle of the true velocity, β :

550

$$551 \quad \tan \beta = \frac{-|v_{\perp_1}| \cos(\phi_{\perp_2}) - |v_{\perp_2}| \cos(\phi_{\perp_1})}{|v_{\perp_1}| \sin(\phi_{\perp_2}) - |v_{\perp_2}| \sin(\phi_{\perp_1})}. \quad (7)$$

552 However, as can be seen in Eqns. (6) and (7), v_{real} and β are sensitive to noise when

553 ϕ_{\perp_1} is approximately equal to ϕ_{\perp_2} . We have therefore opted to leave a more complete

554 implementation of this method as future work. For the present analysis, we assume $v_{real} =$

555 $v_{\perp_1} = v_{\perp_2}$ and use temporal averaging of motion vectors. This is expected to produce

556 approximately correct direction vectors, since detected velocities are distributed about v_{real} ,

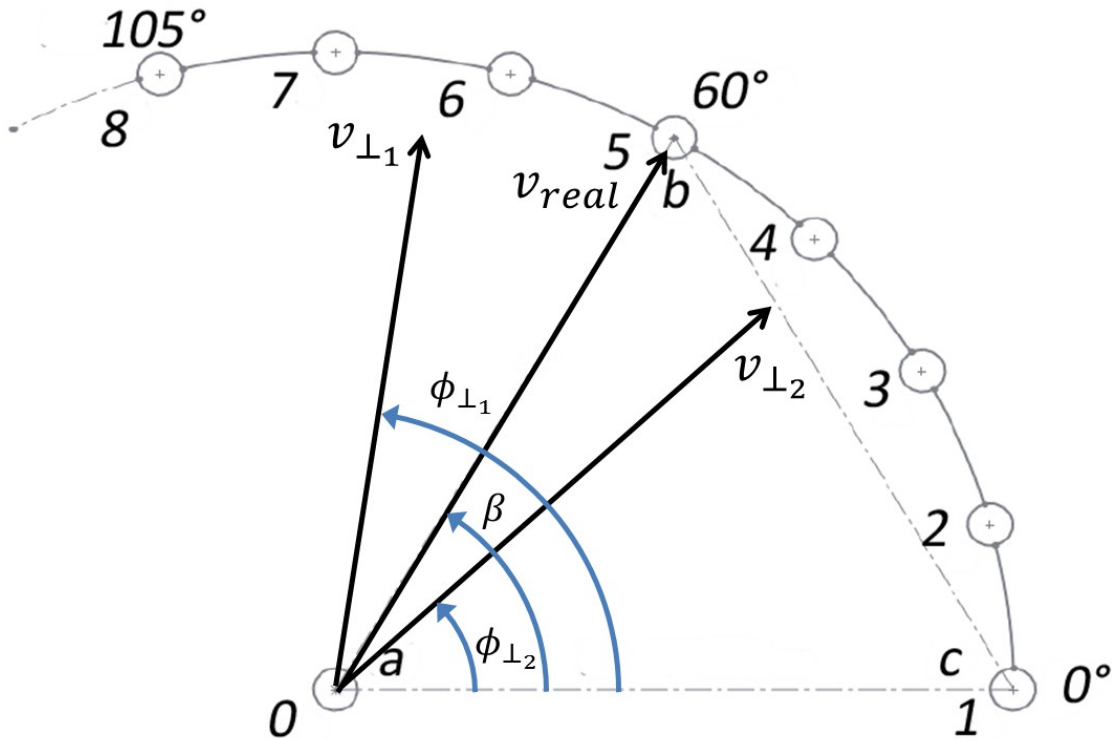
557 but systematically underestimates the speed (vector magnitude) slightly, because all potential

558 v_{\perp} are shorter than v_{real} . The underestimation varies quantitatively depending on the

559 cosine of the cloud edge orientation bias as per Eqn. 6.

560

561



562

563 Fig. 13: Determining real cloud velocity from perpendicular components. v_{real} is real cloud speed with
 564 angle of β in reference to horizontal line (a-c). $v_{\perp 1}$ and $v_{\perp 2}$ are the CMVs perpendicular to the
 565 detected cloud edge from two different passing clouds, and their angles are $\phi_{\perp 1}$ and $\phi_{\perp 2}$ in
 566 reference to line (a-c), respectively.

567

568

569 The original LCE method was developed by Bosch et al. (2013) for a sensor triplet in any non-
 570 linear configuration and spacing and CMVs are solved by geometric-kinematic equations based
 571 on the cloud arrival time at different sensors. While the sensor setup differs, the basic kinematic
 572 analysis of the original LCE method and the LCE-CFM that relies on LCE assumption is similar; a
 573 linear cloud edge passes over the sensors and causes different arrival times based on sensor
 574 arrangements relative to the CMVs. But two main differences do exist between two methods. i)
 575 The original LCE method develops equations to solve two unknowns—speed and direction—using
 576 two data points. In contrast, the LCE-CFM uses 12 data points to solve for the same two
 577 unknowns. The resulting system is over-defined and therefore more tolerant to signal noise. This
 578 also explains why the original LCE method requires low noise signals and multiple quality
 579 controls to produce less scattered results but the LCE-CFM has more clustered CMV raw
 580 measurements without post-filtering. ii) As discussed above, the original LCE method provides a
 581 mechanism to account for the impact of CMV not being perpendicular to the cloud edge, while
 582 the LCE-CFM method returns the CMV perpendicular to the cloud edge. The difference is
 583 summarized in Table 2.

584

585 Table 2: Performance comparison between the original LCE and proposed LCE-CFM method.

	Original LCE	LCE-CFM
CMV distribution	High noise and scattered raw data	Low noise and clustered raw data
CMV limitation	None	Detect the CMV only perpendicular to the cloud edge

586

587

588

5895. Discussion and Conclusions

590

591The principal objective of this research is to introduce a combination of sensors and an algorithm
592to provide an accurate local CBH for sky imager solar forecasting. The combination of a cloud
593speed sensor and sky imager makes measurements of CBH more affordable and convenient
594compared to a ceilometer. Ceilometers cost about US\$20k while the bill of materials for the CSS
595is less than US\$400. Furthermore, a CSS could be directly integrated into the enclosure of a sky
596imager avoiding the need for a separate setup site, power and Ethernet connectivity. In contrast,
597a ceilometer is bulky and requires separate infrastructure.

598

599Firstly, the linear cloud edge assumption of Bosch et al. (2013) is leveraged to propose a method
600(LCE-CFM) for CSS measurements. The method analyzes the similarity, i.e. the correlation, of
601luminance signals between pairs of sensors aligned in different directions. Unlike the original CSS
602method that only considered the time delay of the most correlated pair, all 12 pairs of sensors
603are utilized to fit a cosine function of cross-correlation time delay versus sensor pair direction.
604The approach is motivated by assuming a linear cloud edge passing over the array of sensors. If a
605good fit is observed, the cloud direction is determined as the angle with the maximum time
606delay of the cloud passage on the cosine curve fit. The cloud speed is then equal to the sensor
607spacing divided by that time delay. The advantages and limitations of the LCE-CFM are
608illustrated. The method is also compared to a prior LCE method proposed by Bosch et al. (2013).

609

610CBH is derived by comparing CSS cloud speed measurements in [m s^{-1}] to cloud pixel speed in
611[pixel s^{-1}] from a single sky imager. Over 27 days, the CSS+USI method shows promising CBH
612results with average RMSD of 126 m and nRMSD of 16.9% compared to on-site ceilometer
613measurements. The CBH accuracy depends on the accuracy of both the CSS cloud speed and the
614USI cloud pixel speed, as well as their mutual agreement. While the cloud pixel velocity is
615identified based on CMVs in the entire sky image, the CSS measures the CMVs just of the clouds
616approaching the sun. This discrepancy limits the CBH accuracy. Also, multiple layers of cloud with
617different direction and/or speed could degrade the performance because both CSS and USI are
618only able to determine cloud speed of a single cloud layer. In addition, the accuracy is restricted
619by the fact that the linear cloud edge assumption requires that the cloud motion vector be
620perpendicular to the cloud edge, which causes an underestimation of cloud speed. Lastly, the
621validation suffers from inconsistent measurement areas: (i) the ceilometer measures clouds
622straight overhead, (ii) the CSS detects the clouds that obscure the sun, and (iii) the USI analyzed
623clouds within its field of view that is typically about 10 km^2 . This could result in inconsistencies
624between the ceilometer and the CBH from the CSS+USI method.

625

626Future efforts will focus on implementation of real cloud velocity estimates from perpendicular

4724

48

627components of two different passing cloud edges. USI cloud speed detection could also be
628improved. For example, a CMV field derived from optical flow (Chow et al. 2015) could provide
629the localized information to associate the CMV of the cloud passing the CSS. Optical flow also
630enables detection of multiple cloud layers as well as their respective cloud pixel speeds. Finally,
631validation under different meteorological conditions more relevant to continental climates would
632further substantiate the general applicability of the method.

633

634Acknowledgements

635We acknowledge the donation of a ceilometer from Lawrence Livermore National Laboratory
636facilitated by Julie Lundquist. We also thank Victor Fung, Juan Luis Bosch, and Dominic Fong for
637assisting with CSS maintenance and operation. Juan Luis Bosch suggested the analysis in
638Appendix A1.

639

640 Appendix A1: Validation of the LCE method

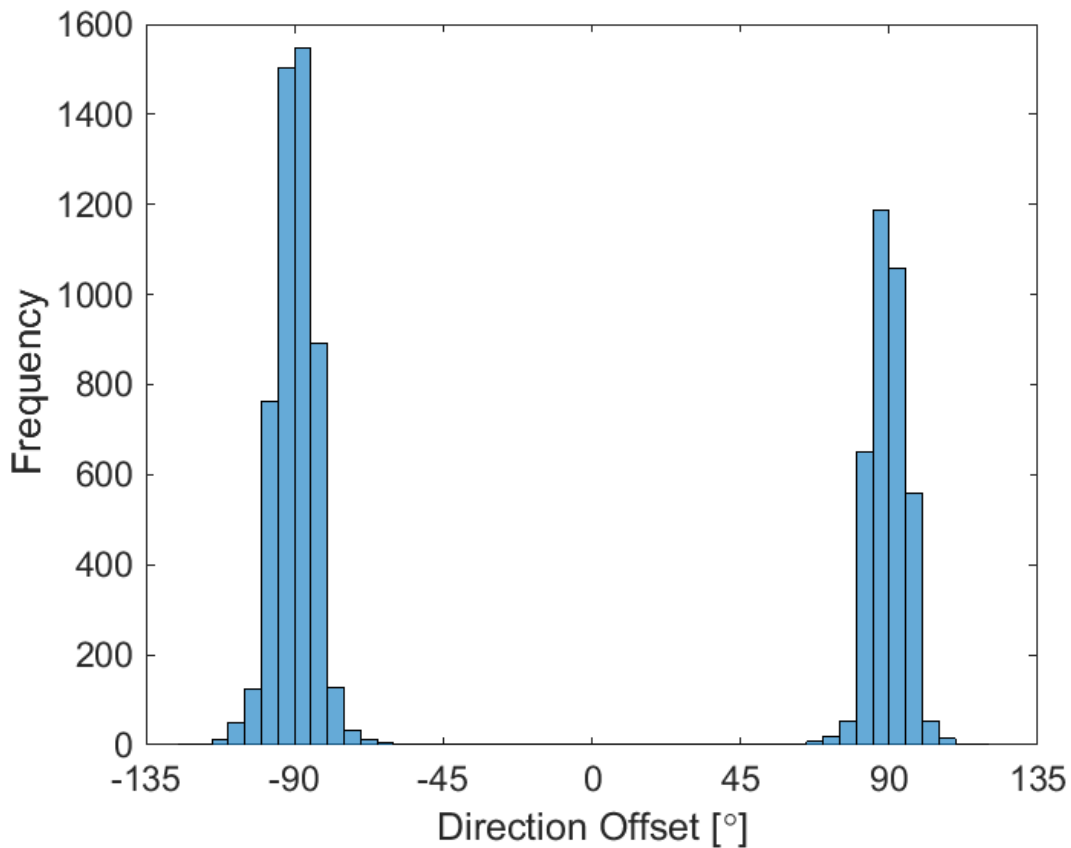
641

642 Fig. A-1 illustrates the direction offset between the direction of 0 s time shift ($\Delta t_{ij}=0$) and
643 the direction that is determined by the LCE-CFM. For example, in Fig. 4, the direction
644 determined by the LCE-CFM method is 322.7° , while the direction closest to 0 s time shift is 240° ,
645 so the offset is -82.74° . Under the LCE assumption, these two directions should always be at
646 right angles to each other; if the cloud edge is not linear, the offset will be larger or smaller
647 depending on the shape of the cloud edge. The calculation is applied to all 27 days analyzed in
648 this paper and the results are plotted in form of histogram in Fig. A-1. Most of the angle offsets
649 are clustered around -90° and $+90^\circ$ which indicates that the data are consistent with the LCE

650 assumption.

651

652



653

654 Fig. A-1: Histogram of LCE assumption validation on all 27 days analyzed in this paper. The y-axis
655 represents the number of CMVs determined by the LCE-CFM using 9-sec segments of CSS data, and the x-
656 axis represents angle offsets between the cloud direction from the LCE-CFM and the direction from the
657 sensor pair which has a time shift closest to zero.

658

659

660

661

662

663

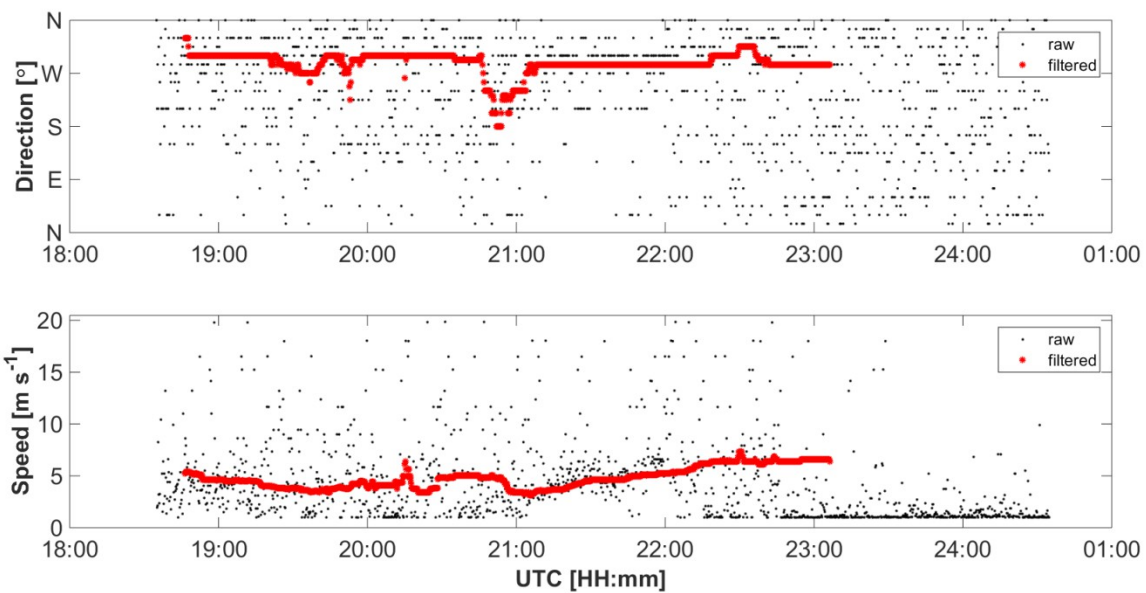
664 Appendix A2: Prior MCP method performance

665

666 Fig. A-2 illustrates that the prior MCP method suffers from some deficiencies as a result of
667 arbitrary correlations from sensor noise, resulting in scattered CMVs outputs. Filtering can
668 address the CMVs variability issue, but at the same time reduces the response of the sensor to
669 sudden changes in cloud velocity. Also, the cloud direction outputs are not continuous as the
670 final direction can only lie along individual sensor pairs.

671

672



673

674 Fig. A-2: An example of the MCP method on July 24, 2013. Black dots show the raw measurement, and red
675 dots show the filtered measurements after moving median filtering.

676

677

678

679

680

681

682

683

684

685

686

687

688

689

690

5327

54

691
692

5528
56

693Appendix A3: Pseudocode

694

695The pseudocode and flowchart (Fig. A3) that show the steps involved to determine local CBH is
 696listed in this section. All acronyms used in pseudocode and flowchart are defined in Table A-3.
 697For the cases when the USI or the CSS output a NaN CMV, or the CSS outputs a CMV that
 698deviates more than 60° from the USI CMV, the algorithm will deliver a NaN CBH. Refer to
 699section 3.2 for the frequency with which NaN CMV is delivered by CSS. The chance that the USI
 700outputs a NaN CMV is only about 3% for partly cloudy days. Since CBH typically changes slowly
 701for conditions with one cloud layer an average of recent results could be used in place of
 702 $CBH_{CSS+USI} = NaN$.

703

704Table A-3: Definition of acronyms used in pseudocode and flowchart. USI is UCSD Sky Imager and
 705CSS is Cloud Shadow Speed Sensor.

$CBH_{CSS+USI}$	CBH derived from CSS measurements and USI cloud pixel speed	USI_{dir}	USI derived cloud direction
CSS_{speed}	CSS measured cloud speed	USI_{pixel}	USI derived cloud pixel speed
CSS_{dir}	CSS measured cloud direction	USI_{speed}	USI derived cloud speed
n	Number of pixels of the cloud map in one dimension	θ_m	Field of view of the USI in degrees from the vertical

706

707

708

709

710

711

712

713

714

715

716

717

718

719

720

721

722

723

724

725

726

5729

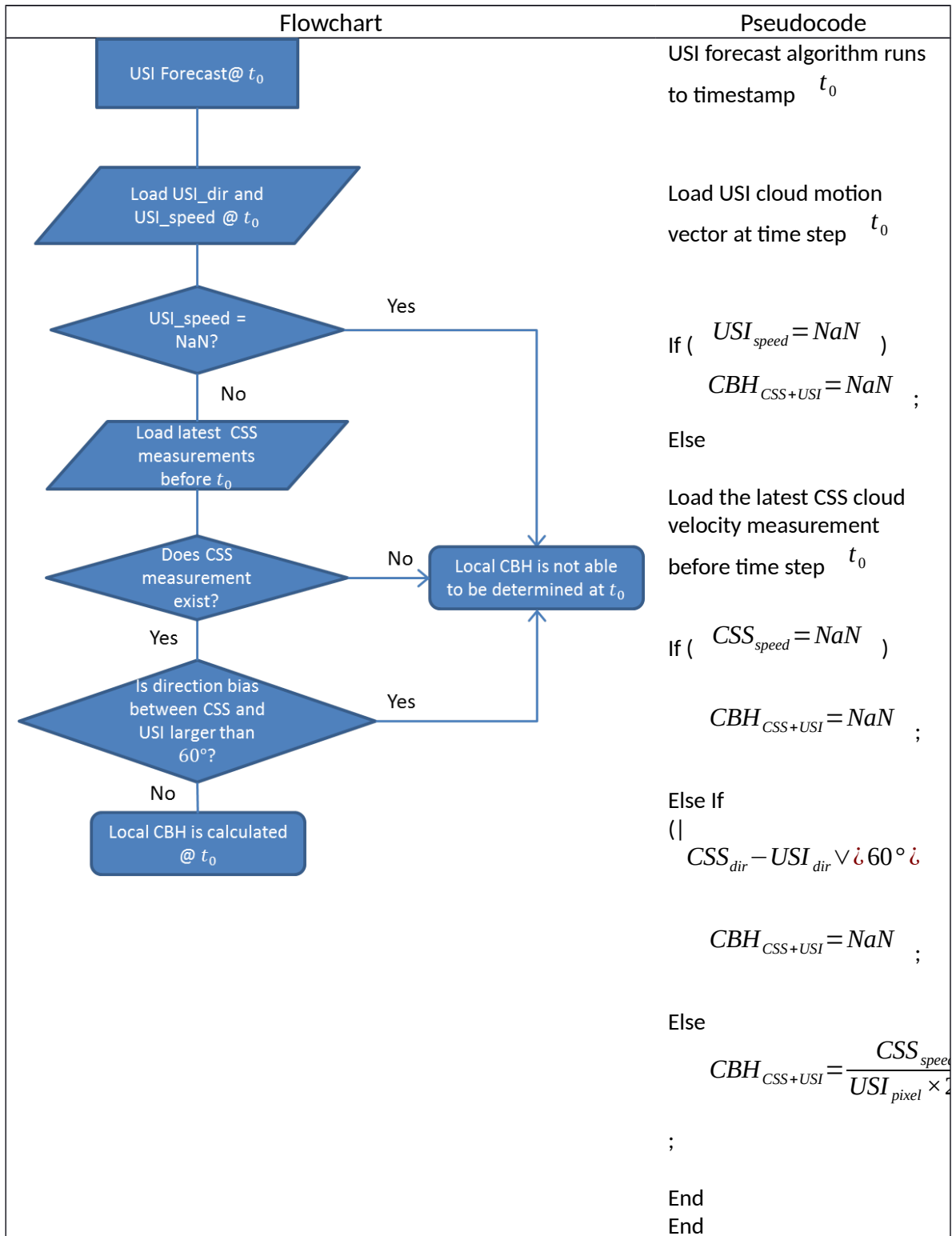
58

727

728

729 Fig. A-3: Flowchart for CBH determination from sky imager and cloud speed sensor.

730



5930

60

731

Move to next timestamp.

6131
62

732References

733

734Allmen, M. C., & Kegelmeyer Jr, W. P. (1996). The computation of cloud-base height from paired
735 whole-sky imaging cameras. *Journal of Atmospheric and Oceanic Technology*, 13(1), 97-
736 113.

737Bosch, J., & Kleissl, J. (2013). Cloud motion vectors from a network of ground sensors in a solar
738 power plant. *Solar Energy*, 95, 13-20.

739Bosch, J. L., Zheng, Y., & Kleissl, J. (2013). Deriving cloud velocity from an array of solar
740 radiation measurements. *Solar Energy*, 87, 196-203.

741Bosch JL, Kleissl J. (2013). Cloud motion vectors from a network of ground sensors in a solar
742 power plant, *Solar Energy*, 95, 13-20.

743Bright, J., Smith, C., Taylor, P., & Crook, R. (2015). Stochastic generation of synthetic minutely
744 irradiance time series derived from mean hourly weather observation data. *Solar Energy*,
745 115, 229-242.

746Cazorla Cabrera, A. (2010). Development of a sky imager for cloud classification and aerosol
747 characterization. Universidad de Granada.

748Chow, C. W., Belongie, S., & Kleissl, J. (2015). Cloud motion and stability estimation for intra-
749 hour solar forecasting. *Solar Energy*, 115, 645-655.

750Chow, C. W., Urquhart, B., Lave, M., Dominguez, A., Kleissl, J., Shields, J., et al. (2011). Intra-
751 hour forecasting with a total sky imager at the UC San Diego solar energy testbed. *Solar*
752 *Energy*, 85(11), 2881-2893.

753Dessler, A., Palm, S., & Spinhirne, J. (2006). Tropical cloud-top height distributions revealed by
754 the ice, cloud, and land elevation satellite (ICESat)/Geoscience laser altimeter system
755 (GLAS). *Journal of Geophysical Research: Atmospheres (1984-2012)*, 111(D12)

6332

64

- 756 Fung, V., Bosch, J., Roberts, S., & Kleissl, J. (2014). Cloud shadow speed sensor. *Atmospheric*
757 *Measurement Techniques*, 7(1), 1693-1700.
- 758 Gaumet, J., Heinrich, J., Cluzeau, M., Pierrard, P., & Prieur, J. (1998). Cloud-base height
759 measurements with a single-pulse erbium-glass laser ceilometer. *Journal of Atmospheric*
760 *and Oceanic Technology*, 15(1), 37-45.
- 761 Ghonima, M., Urquhart, B., Chow, C., Shields, J., Cazorla, A., & Kleissl, J. (2012). A method for
762 cloud detection and opacity classification based on ground based sky imagery.
763 *Atmospheric Measurement Techniques*, 5(11), 2881-2892.
- 764 Kassianov, E., Long, C. N., & Christy, J. (2005). Cloud-base-height estimation from paired
765 ground-based hemispherical observations. *Journal of Applied Meteorology*, 44(8), 1221-
766 1233.
- 767 Killius, N., Prah, C., Hanrieder, N., Wilbert, S., & Schroedter-Homscheidt, M. (2015) *On the use*
768 *of NWP for Cloud Base Height Estimation in Cloud Camera-Based Solar Irradiance*
769 *Nowcasting. ICEM 2015, 23.-26. June 2015, Boulder, USA.*
- 770 Liu, L., Sun, X., Liu, X., Gao, T., & Zhao, S. (2015). Comparison of cloud base height derived
771 from a ground-based infrared cloud measurement and two ceilometers. *Advances in*
772 *Meteorology*.
- 773 Martucci, G., Milroy, C., & O'Dowd, C. D. (2010). Detection of cloud-base height using Jenoptik
774 CHM15K and Vaisala CL31 ceilometers. *Journal of Atmospheric and Oceanic Technology*,
775 27(2), 305-318.
- 776 Nguyen, D. A., & Kleissl, J. (2014). Stereographic methods for cloud base height determination
777 using two sky imagers. *Solar Energy*, 107, 495-509.
- 778 Prata, A., & Turner, P. (1997). Cloud-top height determination using ATSR data. *Remote Sensing*
779 *of Environment*, 59(1), 1-13.

780Schmidt, T., Kalisch, J., Lorenz, E., & Heinemann, D. (2015). Evaluating the spatio-temporal
781 performance of sky imager based solar irradiance analysis and forecasts. *Atmospheric*
782 *Chemistry and Physics Discussions*, 15(19), 26997-27039.

783Shaw, J. A., & Nugent, P. W. (2013). Physics principles in radiometric infrared imaging of clouds
784 in the atmosphere. *European Journal of Physics*, 34(6), S111-S121.

785Urquhart, B., Kurtz, B., Dahlin, E., Ghonima, M., Shields, J., & Kleissl, J. (2015). Development of
786 a sky imaging system for short-term solar power forecasting. *Atmospheric Measurement*
787 *Techniques*, 8, 875-890.

788Wang, J., & Rossow, W. B. (1995). Determination of cloud vertical structure from upper-air
789 observations. *Journal of Applied Meteorology*, 34(10), 2243-2258.

790Yang, H., Kurtz, B., Nguyen, D., Urquhart, B., Chow, C. W., Ghonima, M., et al. (2014). Solar
791 irradiance forecasting using a ground-based sky imager developed at UC San Diego. *Solar*
792 *Energy*, 103, 502-524.